JOURNAL OF APPLIED ELECTROCHEMISTRY 20 (1990) 1–10

A model of zinc–nickel alloy electrodeposition in an industrial-scale cell

M. F. MATHIAS*, C. M. VILLA, T. W. CHAPMAN

Department of Chemical Engineering, University of Wisconsin, Madison, Wisconsin 53706, USA

Received 6 March 1989; revised 16 June 1989

This paper analyses continuous alloy plating of steel strip with the use of a rate model that accounts for migration and homogeneous equilibria in the mass-transport boundary layer adjacent to the cathode. The model predicts the effect of bath composition, temperature, electrolyte velocity, and current density on the alloy composition and current density distribution within the cell. The effect of a slight taper of the interelectrode gap was also considered. The results were used to evaluate which of several currently used electrogalvanizing cells are most likely to succeed in producing coats of uniform zinc–nickel alloy composition. It is demonstrated that mass-transfer of the zinc is a critical factor under typical industrial conditions and that electrolyte injection counter to the strip movement is important for application of an electrodeposit uniform in composition.

Nomenclature

A	electrode area (cm^2)
c_i	concentration of species i ($mol\,cm^{-3}$)
d_e	equivalent diameter (cm)
D_i	diffusion coefficient of species i ($cm^{-2}\,s^{-1}$)
E'	formal potential (V)
F	Faraday's constant, 96487 $C\,mol^{-1}$
f	F/RT (mole (equiv V)$^{-1}$)
ΔH_s^*	apparent heat of activation ($J\,mol^{-1}$)
i	current density ($A\,cm^{-2}$)
k	mass-transfer coefficient ($cm\,s^{-1}$)
k_s	standard rate constant ($cm\,s^{-1}$)
K_m	cumulative equilibrium constant
L	length of plating cell (cm)
m	degree of complexation
N_i	molar flux of species i ($mol\,cm^{-2}\,s^{-1}$)
NC	number of components
R	gas constant, 8.314 $J\,mol^{-1}\,K^{-1}$
Re	Reynolds number, ud_e/v
$\bar{R}_i$	production rate due to homogeneous reactions ($mol\,cm^{-3}\,s^{-1}$)
S	interelectrode distance (cm)
Sc	Schmidt number, v/D_R
Sh	Sherwood number, kd_e/D_R
T	absolute temperature (K)
u	characteristic velocity ($cm\,s^{-1}$)
u_i	mobility of species i ($cm^2\,mol\,J^{-1}\,s^{-1}$)
v	electrolyte velocity ($cm\,s^{-1}$)
V	electrode potential (V)
w_i	quadrature weight at point i
W	width of plating cell (cm)
x	axial coordinate
X_m	mole fraction of metal M in alloy
Y	transverse coordinate
z_i	charge on species i
α_c	cathodic transfer coefficient
δ	mass-transfer boundary-layer thickness (cm)
κ	solution conductivity ($\Omega^{-1}\,cm^{-1}$)
ν	kinematic viscosity ($cm^2\,s^{-1}$)
Φ	potential in solution (V)
Γ	left-hand side of Equation 17

Subscripts

b	bulk value
dev	developed flow region
ent	entrance length region
M	metal species, Ni or Zn
o	interfacial condition
R	reference species on which δ is based
tran	transition point from entrance to developed flow regions
x	dependent on axial position

1. Introduction

Increased production of continuously electrogalvanized steel sheet in the last five years has been due in large part to demand by automakers [1]. The forecast is for increasing demand with continued interest in alternative products, such as zinc–nickel alloy coated steel sheet which, with coating compositions of approximately 10 mol % nickel, can provide better corrosion resistance than the galvanized product [2]. In fact, existing steel-strip electrogalvanizing plants may be used increasingly for alloy deposition. Models of electrogalvanizing cells have been developed (e.g. [3a]); however, there are no models of industrial-scale alloy plating cells published, primarily because the required kinetic parameters are not known. In this paper, we employ a kinetic model for zinc–nickel alloy deposition identified in a lab-scale study [4] combined with a film model of the mass-transfer boundary layer near the cathode to simulate zinc–nickel alloy deposition in an

* Present address: Mobil Research and Development Corporation, Paulsboro, New Jersey 08066-0480, USA.

0021-891X/90 $03.00 + .12

industrial-scale parallel-plate cell. The model accounts for the effects of operating variables on alloy composition and uniformity and paves the way for design and optimization. Based on the similarities between the parallel-plate geometry and the cells in use for industrial electrogalvanizing, the model results were used to analyse the capability of various electrogalvanizing cells to serve as alloy plating cells.

Coils of steel sheet are supplied to strip-plating processes in widths of 50 to 180 cm with sheet thicknesses of 0.065 to 0.165 cm. The strip is unwound and fed rapidly (2 to 4 m s^{-1}) through an electrolytic alkaline cleaner and an acid dip, plated, rinsed, dried, and rewound for shipping to the consumer.

Schematics of two currently used electrogalvanizing cells are shown in Fig. 1. They represent cells installed in four of the five electrogalvanizing plants brought on line in the United States in 1986 [3b–d]. Figure 1a shows a vertical cell with countercurrent electrolyte injection which serves to improve mass transfer and remove gas bubbles. In the gravity-flow cell shown in Fig. 1b, electrolyte flows out of a weir just above each anode, filling the gap between the anode and the passing strip. During typical operation, the interelectrode electrolyte velocity is approximately 3 to 4 m s^{-1}. In general the top of the anode is positioned slightly further away from the strip (about 9 mm) than the bottom (about 7 mm) in order to form a V-shape which helps to hold the liquid between the two electrodes. After passing through the interelectrode gap, the electrolyte drains to a holding tank not shown in the schematic. One- or two-sided plating can be conducted with these two cell types, and approximately 15 to 20 cells are operated in series in order to achieve the desired deposit thickness (around 15 μm). Insoluble gas evolving or soluble zinc anodes can be employed.

The geometry of the cells shown in Fig. 1 can be approximated by that of the parallel-plate cell. However, the mass transfer in the channel, because of Couette flow induced by the moving strip, is more complicated than the stationary electrode case, and mass-transfer correlations are unavailable. In this paper, we resort to analysing turbulent flow past two parallel plates using available correlations for estimates of the mass-transfer boundary layer thickness. A film model of the mass-transport, including the effects of migration and chloride complexing of the zinc, was applied locally along the length of the cathode. The applicability of this model to the more complicated industrial-scale problem will be discussed.

Table 1. Nickel–zinc plating baths used in this study

	Roehl bath	*Modified Roehl bath*
Contents		
$ZnCl_2$	0.92 M	0.57 M
$NiCl_2$	0.57 M	0.92 M
Acetic acid	0.366 M	0.366 M
Total metal	1.49 M	1.49 M
Ni/total metal	0.38	0.62
Properties		
pH at 25° C†	1.6	1.6
Conductivity (Ω^{-1} cm^{-1})†		
30° C	0.0946	0.109
40° C	0.105	0.123
50° C	0.116	0.137
Kinematic viscosity (cm^2 s^{-1})‡		
30° C	0.0117	0.0117
40° C	0.00934	0.0934
50° C	0.00782	0.00782

* Based on patent by Roehl and Dillon [5].
† Measured.
‡ Measured at 25° C and assumed to have the same temperature dependence as water.

2. Model development

Figure 2 shows the parallel-plate geometry on which

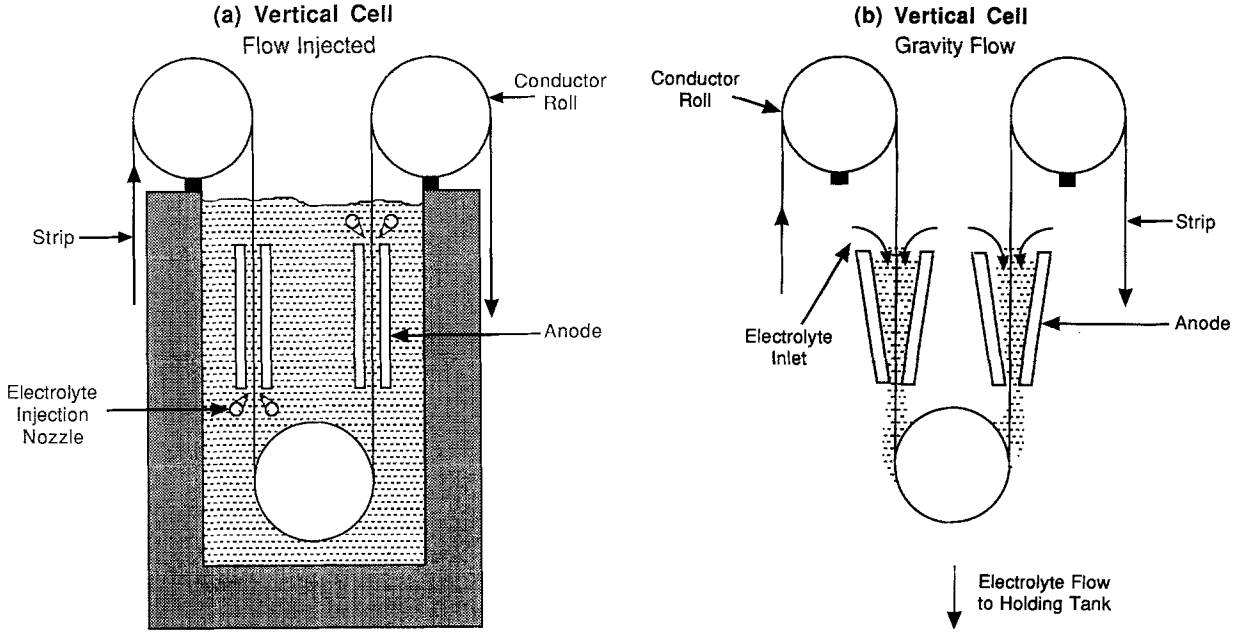

Fig. 1. Schematic diagrams of two cell types used in United States continuous strip electrogalvanized lines started up in 1986.

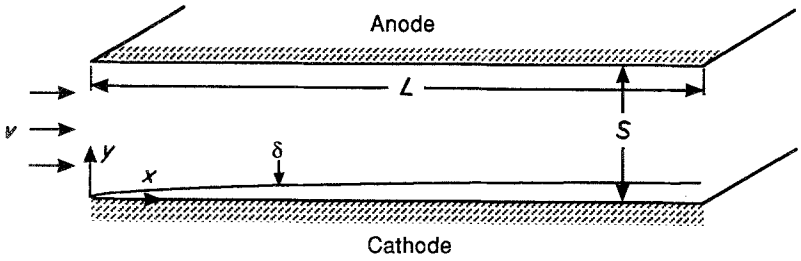

Fig. 2. Diagram of the parallel-plate cell geometry on which the alloy-plating model is based.

the model is based, with cell length L, width W, and interelectrode gap S. The axial coordinate is represented by x and the coordinate normal to the electrodes by y. Electrolyte is considered to be flowing between the stationary electrodes in the x direction with velocity v.

2.1. *Electrolyte composition and complexation*

Table 1 shows contents and properties of the two alloy plating baths that were considered. The Roehl bath is based on the recommendations of Roehl and Dillon's 1971 patent [5]. In the modified Roehl bath, the concentrations of the zinc and nickel chlorides are reversed, keeping the total metal concentration constant.

Migration effects depend strongly on the concentrations and charges of the species in the solution. As in our earlier work with this system [4, 6], zinc complex formation constants reported by Schukarev *et al.* [7], obtained under conditions most closely resembling those present here, were used. Because the baths are very acidic, zinc hydroxide equilibria are not significant. For zinc chloride complexing, the cumulative equilibrium constant, K_m, is defined by

$$K_m = \frac{[ZnCl_m^{(+2-m)}]}{[Zn^{2+}][Cl^-]^m} \qquad m = 1, 2, 3, 4 \quad (1)$$

where m is the degree of complexation. Table 2 summarizes the homogeneous equilibrium results for the Roehl and modified Roehl baths.

2.2. *Electrode kinetics*

The kinetics model and parameter values determined from the lab-scale experiments [4] were used to provide the electrode kinetics expressions in the alloy deposition model. The mathematical forms are based on independent two-step mechanisms for each of the metal deposition reactions. They are represented for the metal M (either Ni or Zn) as

$$MCl_m^{(+2-m)} + e^- \longleftrightarrow M^+ + mCl^- \qquad m = 0, 1, 2, 3, \text{ or } 4 \quad (2)$$

$$M^+ + e^- \longleftrightarrow M \quad (3)$$

where m is here the coordination number of the electroactive species. For nickel, assumed to exist only as a free ion, m is zero, and zinc deposition is assumed to occur through only one species. When the first step in the mechanism is assumed to be rate determining for each metal deposition sequence, the partial current density i_M for each reaction is given by

$$\frac{i_M}{2F} = \frac{i_{M1}}{F} = k_{s,M} \times (\exp\{(2 - \alpha_{c,M}) f(V - \Phi_0 - E'_M)\} X_M [Cl^-]_0^m - \exp\{-\alpha_{c,M} f(V - \Phi_0 - E'_M)\} [MCl_m^{(+2-m)}]_0) \quad (4)$$

where $k_{s,M}$ and $\alpha_{c,M}$ are, respectively, the standard rate constant and cathodic transfer coefficient for metal reaction M, f represents F/RT, and $V - E'_M$ is the cathode potential. The interfacial concentrations, given by the bracketed quantities, the mole fraction of the metal, X_M, and the interfacial solution potential, Φ_0, are functions of axial position along the electrode, as is the resulting local partial current. The potential Φ_0 is referenced to a potential datum in the solution adjacent to the anode. The local nickel mole fraction in the alloy can be calculated using the predicted partial currents and an application of Faraday's law as

$$X_{Ni} = \frac{i_{Ni}}{i_{Ni} + i_{Zn}} \quad (5)$$

The kinetics parameters and reactant zinc species identified in lab-scale studies [4, 6] are listed in Table 3. The standard rate constants were adjusted for the effect of temperature using the equation

$$k_s = k_{s,298} \exp\left(\frac{-\Delta H_s^*}{R}\left(\frac{1}{T} - \frac{1}{298}\right)\right) \quad (6)$$

where $k_{s,298}$ is the rate constant at 298 K, and ΔH_s^* is the apparent activation energy. No temperature

Table 2. Cumulative formation constants and calculated equilibrium concentrations in solutions of Ni and Zn chloride

Species	*Formation constant*	*Concentration (M)*	
		Roehl	*Modified Roehl*
Zn^{2+}		0.213	0.0663
$ZnCl^+$	0.48*	0.112	0.0469
$ZnCl_2$	0.89*	0.230	0.128
$ZnCl_3^-$	0.50*	0.143	0.106
$ZnCl_4^{2-}$	0.71*	0.222	0.222
Ni^{2+}		0.57	0.92
Cl^-		1.101	1.473

* Zinc constants from Schukarev *et al.* [7].

Table 3. Parameters used in kinetic model

	Nickel	*Zinc*
k_s (cm s^{-1}) @ 298 K†	6.31×10^{-8}	1.59×10^{-3}
α_c†	0.29	0.40
Reacting species†	Ni^{2+} ($m = 0$)	$ZnCl_3^-$ ($m = 3$)
E' (V w.r.t. SCE)	−0.494‡	−0.9911§
ΔH_s^* (J mol^{-1})¶	108.4	111.7

† Taken from [4].
‡ Taken from [8].
§ Adjusted from −1.000 V [8] to account for $ZnCl_3^-$ as reacting species.
¶ Taken from [6].

dependence of the formal potentials was accounted for owing to lack of available data.

The kinetics expressions are dependent on the interfacial potential and the interfacial electroactive species concentrations. The Laplace equation must be solved to provide the former, and a model of the mass-transfer boundary layer is required to give the latter. Each of these components of the model will be discussed below.

2.3. *Potential distribution*

Calculation of the potential distribution is simplified significantly by ignoring edge effects at the strip edges and at the entrance and exit of the cell. This is justified for analysis of industrial cells because the cell length and width are large relative to interelectrode gap. We also ignored the effect of the finite strip resistance, a factor when plating high-gauge steels [3a]. When the strip resistance is negligible, the interelectrode gap constant, and edge effects are ignored, the primary and secondary current distributions are uniform.

The potential distribution in a uniform electrolyte is described by the Laplace equation. Because the length dimension of the cell is large relative to the interelectrode gap, the potential gradient in the y direction was assumed to be much larger than the variation in the x direction. The Laplace equation, assuming no variations in the width dimension, becomes simply

$$\frac{\partial^2 \Phi}{\partial y^2} = 0 \tag{7}$$

The voltage balance was based on the assumption of an isopotential surface in the solution adjacent to the anode. This is generally associated with the assumption of a reversible anode, but it is also valid when the surface and concentration overpotentials are constant along the anode. Using the potential in the electrolyte adjacent to the anode as the zero-potential datum, the solution to the Laplace equation is

$$\Phi = \left(1 - \frac{y}{S}\right) \Phi_0 \tag{8}$$

where Φ_0 is the potential in the solution immediately adjacent to the cathode. Application of Ohm's law allows the calculation of the surface potential as a function of the total current

$$\Phi_0 = \frac{i_{Tot}\, S}{\kappa} \tag{9}$$

where κ is the specific conductivity of the electrolyte, S is the interelectrode distance, and i_{Tot} is the local current density (negative when cathodic). In summary, the potential gradient is predicted to be linear in y with the current lines running perpendicular to the electrodes.

Equation 9 was used for calculation of the interfacial potential needed in the kinetic relation (Equation 4), neglecting the small potential variation due to conductivity changes in the mass-transfer boundary layer as well as the diffusion potential associated with the concentration gradient. The conductivity was considered to be a constant and unaffected by gas evolution at either electrode — oxygen on the insoluble anode or hydrogen on the cathode. The contribution of the hydrogen reduction to the total current was assumed to be negligible; in practice, reported metal deposition current efficiency for zinc–nickel deposition varies between 85 and 100%.

2.4. *Mass transfer*

The Reynolds number for this geometry is given by

$$Re = \frac{d_e u}{\nu} \tag{10}$$

where ν is the kinematic viscosity, u is the characteristic (electrolyte) velocity and d_e is the equivalent diameter which is given by

$$d_e = \frac{4WS}{2(W + S)} \tag{11}$$

In commercial cells $W \gg S$, and d_e reduces to $2S$.

Using a typical industrial strip speed of 3.3 m s^{-1} as the characteristic velocity, the Reynolds number for an industrial cell configuration is approximately 2×10^5. Thus the flow is turbulent, and the mass-transfer effects can be assumed to be located in a thin boundary layer close to the electrode.

In the entrance to the cell where fresh electrolyte is injected, the concentrations of the metal ions at the electrode surface are equal to the bulk concentrations. The current that passes early in the residence time in the cell will deplete the laminar sublayer of reacting ions, until the resulting mass-transfer boundary layer grows out to a point where the mass transfer by turbulent convection becomes significant. Downsteam of this point, the mass-transfer boundary-layer thickness will be determined by the degree and nature of the turbulence. In a parallel-plate cell, mass-transfer entrance-length effects are generally thought to be negligible at a downstream distance of 10 equivalent diameters [9].

2.4.1. Mass-transfer correlations employed. Near the entrance to the cell, during the initial depletion of the boundary layer, penetration theory can be used to

give an estimate of the mass-transfer coefficient. This estimate can be expressed in terms of dimensionless groups as follows

$$Sh_x = \left(\frac{kx}{D_R}\right) = a\,(Re_x Sc)^{1/2} \qquad (12)$$

where Sh_x is the local Sherwood number, k is the local mass-transfer coefficient, and D_R is the diffusion coefficient on which the mass-transfer coefficient is based. The Reynolds number is based on x, the distance down the electrode, and Sc is the Schmidt number. When the wall concentration of the reacting species is constant, the coefficient a in Equation 12 is equal to 0.564 [10], and when the flux is constant, a is 0.886 [11]. Assuming that k is related to a boundary-layer thickness δ as D_R/δ, we can eliminate k from Equation 12 and generate an equation to estimate the film thickness in the entrance region

$$\delta = \frac{x}{a}\,(Re_x\, Sc)^{-1/2} \qquad (13)$$

This predicts a film thickness that increases with axial position as would be expected.

When the turbulence determines the diffusion layer thickness, the well known Chilton–Colburn correlation [9] can be used for an estimate of the mass-transfer coefficient

$$Sh = \left(\frac{k\,d_e}{D_R}\right) = 0.023\; Re^{4/5}\; Sc^{1/3} \qquad (14)$$

where the characteristic distance is now the equivalent diameter. This predicts a uniform mass-transfer coefficient independent of position along the electrode. Using again the estimation of k equal to D_R/δ and inserting it in Equation 14 yields an estimate of the mass-transfer boundary-layer thickness

$$\delta = \frac{d_e}{0.023}\, Re^{-4/5}\; Sc^{-1/3} \qquad (15)$$

in the fully turbulent region.

We estimated the entrance length as the distance along the electrode at which Equation 13 predicts the same film thickness as Equation 15. This transition distance, $(x/L)_{tran}$, is given by

$$\left(\frac{x}{L}\right)_{tran} = b\; Re^{-3/5}\; Sc^{1/3}\left(\frac{d_e}{L}\right) \qquad (16)$$

where b is 601.7 for the constant surface concentration and 1485 for the constant flux situation.

For the system and conditions studied here, the constant concentration equation yields entrance length predictions from Equation 16 that are between 5 and 10 equivalent diameters, whereas the constant flux transition is predicted to be from 12 to 25 equivalent diameters along the cell length. Because the former yields predictions of the entrance length that are more consistent with the previously reported value of approximately 10 [9], the constant concentration correlation was used in the model. Upstream of the transition distance, the penetration model, Equation 13, was used to estimate the mass-transfer boundary-layer thickness, and the Chilton–Colburn analogy, Equation 15, was used downstream.

2.4.2. Application of this transport model to industrial-scale cells. In industrial continuous strip-plating cells, the flow regime is turbulent Couette flow in a channel, characterized by one surface moving relative to a stationary one. When the electrolyte is injected this flow pattern is further modified depending on the electrolyte velocity and the point of injection with respect to strip movement [12].

Sakiadis [13] has analysed both laminar and turbulent Couette flow of a strip moving through a stagnant infinite fluid and presented the average friction factor as a function of Reynolds number based on the velocity of the strip and the length down the moving surface. Using his results and the j factor analogy produces an equation in the form of Equation 12 with a leading coefficient of 0.444, and exponents of $\frac{1}{2}$ on Re_x and $\frac{1}{3}$ on Sc. With a Schmidt number of 1000, this leads to prediction of the boundary-layer thickness about three times that given by Equation 13. For the turbulent case, Sakiadis's results lead to an expression with exponents on Re and Sc identical to those in Equation 14 with a leading coefficient of 0.023 and an additional d_e/x factor raised to the $\frac{1}{5}$ power. At the end of a typical industrial plating cell where d_e/x is equal to 0.02, this predicts boundary-layer thicknesses twice that predicted by Equation 15. Thus, there is reasonably good agreement between correlations determined for electrolyte flow in a channel and those determined for Couette flow in an infinite solution. This suggests that, for the sake of applying the results of the model to the industrial cell, it is reasonable to employ the channel flow correlations and consider the characteristic velocity, u, as the relative velocity between the strip and the electrolyte.

2.4.3. Film model. The one-dimensional steady-state conservation of mass equation, assuming applicability of dilute solution equations and considering diffusion and migration, can be written as

$$D_i \frac{\partial^2 c_i}{\partial y^2} + z_i u_i F\left(c_i \frac{\partial^2 \Phi}{\partial y^2} + \frac{\partial c_i}{\partial y} \times \frac{\partial \Phi}{\partial y}\right) = \bar{R}_i \qquad (17)$$

for each solute species i. The dependent variables are given by c, the concentration, and Φ, the local potential in the solution. Physical properties for species i are represented by D_i, the diffusivity, and u_i, the ionic mobility. R_i is the net production rate of species i due to homogeneous reactions and z_i is the charge on species i. The electroneutrality condition

$$\sum_{i=1}^{NC} c_i z_i = 0 \qquad (18)$$

where NC is the number of ionic species, is also applied in the boundary layer.

Homogeneous metal–ligand exchange reactions are

characteristically labile, so we assumed that homogeneous equilibrium is maintained among the zinc complexes. To incorporate simultaneous equilibria in the mass-transfer boundary layer, the conservation equations can be combined to eliminate the homogeneous rate terms. This yields the following three elemental transport equations where Γ represents the left-hand side of Equation 17: a mass balance on the chloride

$$\Gamma(c_{Cl^-}) + \Gamma(c_{ZnCl^+}) + 2\Gamma(c_{ZnCl_2}) + 3\Gamma(c_{ZnCl_3^-}) + 4\Gamma(c_{ZnCl_4^{2-}}) = 0 \quad (19)$$

a mass balance on the zinc

$$\Gamma(c_{Zn^{2+}}) + \Gamma(c_{ZnCl^+}) + \Gamma(c_{ZnCl_2}) + \Gamma(c_{ZnCl_3^-}) + \Gamma(c_{ZnCl_4^{2-}}) = 0 \quad (20)$$

and a mass balance on the nickel, which is not involved in any extensive homogeneous reactions

$$\Gamma(c_{Ni^{2+}}) = 0 \quad (21)$$

In addition to these three equations, the four equilibrium expressions for the zinc chloride species (Equation 1) and the electroneutrality condition are applied in the boundary layer to compute the concentration and potential profiles.

Boundary conditions at the electrode match the electrode reaction stoichiometry with the fluxes of the solute species at the electrode. For species i, the flux is given as

$$N_i = -D_i \left.\frac{\partial c_i}{\partial y}\right|_{y=0} - z_i u_i F c_i \left.\frac{\partial \Phi}{\partial y}\right|_{y=0} \quad (22)$$

in which the two contributions to the flux N are from diffusion and migration, respectively.

Because of the instantaneous interconversion between species in equilibrium in the solution, elemental-flux boundary conditions must be used. The transformation is analogous to that carried out above for the conservation equations. The elemental zinc flux is proportional to the zinc partial current and is given by

$$\frac{i_{Zn}}{2F} = N_{Zn^{2+}} + N_{ZnCl} + N_{ZnCl_2} + N_{ZnCl_3^-} + N_{ZnCl_4^{2-}} \quad @ \quad y = 0 \quad (23)$$

the elemental nickel flux by

$$\frac{i_{Ni}}{2F} = N_{Ni^{2+}} \quad @ \quad y = 0 \quad (24)$$

and, finally, chloride which has no net flux into the electrode

$$N_{Cl^-} + N_{ZnCl^+} + 2N_{ZnCl_2} + 3N_{ZnCl_3^-} + 4N_{ZnCl_4^{2-}} = 0 \quad @ \quad y = 0 \quad (25)$$

As in the interior region, the four zinc equilibrium expressions and the electroneutrality condition provide the remaining boundary conditions at the electrode.

For the boundary conditions at the outer edge of the film, the bulk concentration value for each species is specified along with the potential calculated from the Laplace equation

$$c_i = c_{b,i} \quad @ \quad y = \delta \quad (26)$$

$$\Phi = \frac{i_{Tot}}{\kappa}(S - \delta) \quad @ \quad y = \delta \quad (27)$$

The bulk concentrations of the reacting species were assumed to be constant along the length of the cell.

Table 4. Transport properties used in model at 25°C

Species	*Diffusivity* (10^5 cm^2 s^{-1})	*Mobility coefficient*‡ $z_i u_i F$ (10^4 cm^2 C^{-1} Ω^{-1})
Ni^{2+}	0.71†	5.49
Zn^{2+}	0.71*	5.49
$ZnCl^+$	0.71	2.75
$ZnCl_2$	0.71	0.0
$ZnCl_3^-$	0.71	−2.75
$ZnCl_4^{2-}$	0.71	−5.49
Cl^-	2.03*	−7.91

* Taken from [14].
† Values for Ni^{2+} and zinc complexes assumed equal to value for Zn^{2+}.
‡ Based on Nernst–Einstein relation, $u_i = D_i/RT$.

The values of the transport properties used are given in Table 4 for 298 K. They are based on infinite-dilution ionic diffusivities tabulated by Newman [14]. The diffusivity for Zn^{2+} was used in the calculation of the mass-transfer boundary-layer thickness. The diffusion coefficients were assumed to vary with absolute temperature to the $\frac{3}{2}$ power.

2.5. *Computational method*

First, Equation 16 was used to estimate the entrance length. Then, the potential, transport, and kinetics equations were solved simultaneously for a specified cathode voltage to provide the local partial current values at selected points along the electrode using two-point orthogonal collocation (plus the two boundary points) based on Lobatto polynomials in the y direction [15]. The average partial current densities within the entrance region were estimated by quadrature based on Legendre polynomials [15] as follows

$$\langle i_M \rangle_{ent} = \frac{1}{2}\sum_{i=1}^{N_{ent}} w_i i_M(x_i) \quad (28)$$

where $\langle i_M \rangle_{ent}$ is the average partial current of metal M in the entrance region, N_{ent} is the number of quadrature points used (normally 6), w_i and x_i are the quadrature weights and locations, respectively. The problem was then also solved in the developed turbulent region to give the partial current densities there, $i_{M,dev}$. The overall average partial current, $\langle i_M \rangle$, was estimated by weighting the average partial currents in the two regions by their fractional electrode lengths as follows

$$\langle i_M \rangle = \langle i_M \rangle_{ent}\left(\frac{x}{L}\right)_{tran} + i_{M,dev}\left(1 - \left(\frac{x}{L}\right)_{tran}\right) \quad (29)$$

The local and average deposit compositions were then calculated using Equation 5. Because it was desired to treat the total current as an independent variable, as is done in control of industrial processes, another single-variable Newton–Raphson technique was applied to iterate on the voltage, V, in order to obtain the solution for a specified total current.

3. Model predictions and discussion

Simulations were run for both the Roehl and the modified Roehl baths at temperatures of 30, 40 and 50° C. The effect of the characteristic velocity was also considered at three levels: 2, 2.75, 3.5 m s^{-1}. Local and average nickel composition values were determined for average current densities from 0.04 to 1.2 A cm^{-2}, based on typical electrogalvanizing operating conditions [3]. An electrode length of 1 m and an inter-electrode gap of 1 cm were used in most calculations. When this gap is constant along the electrode, the corresponding current density is also essentially constant. This occurs because the electrolyte resistance is uniform and dominates the overall cell resistance. In fact the difference between the minimum and maximum local current density was generally less than 2%. The calculated potential gradient in the y direction was typically 50 000 times that in the x direction, supporting the assumption of parallel current lines perpendicular to the cathode. The potential variation from the Laplace prediction due to concentration variations within the boundary layer was also confirmed to be negligible. Finally, a macroscopic mass balance on the system showed that the bulk concentrations remain unchanged throughout the reactor.

3.1. *Average nickel composition results*

3.1.1. Effect of characteristic velocity. The effect of the characteristic velocity and the total current density on the average alloy composition can be seen in Fig. 3 for the modified Roehl bath at 40° C. The infinite strip speed result represents the hypothetical situation of an infinite mass-transfer coefficient, where there is no depletion of the reacting species at the electrode regardless of the current level. Increasing the current under these secondary current distribution conditions decreases the nickel content in the alloy, drastically at low total currents and more gradually at larger currents. At characteristic velocities equal to practical industrial strip speeds the zinc becomes mass-transfer-limited within this current range, and the resulting tertiary current distribution shows an increase in average nickel composition with increasing current. The slower the characteristic velocity, the more drastic the mass-transfer effect and the more rapid the increase in the nickel composition with increasing current.

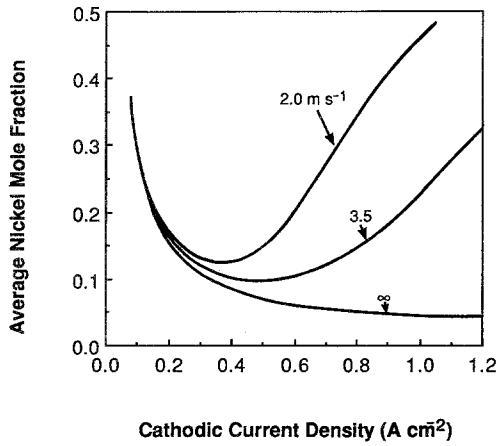

Fig. 3. Effect of the characteristic velocity and the average current density on the axially averaged nickel composition in the alloy for the modified Roehl bath at 40° C. Results are shown for velocities of 2.0 and 3.5 m s^{-1} as well as for infinite strip speed, the secondary current distribution case.

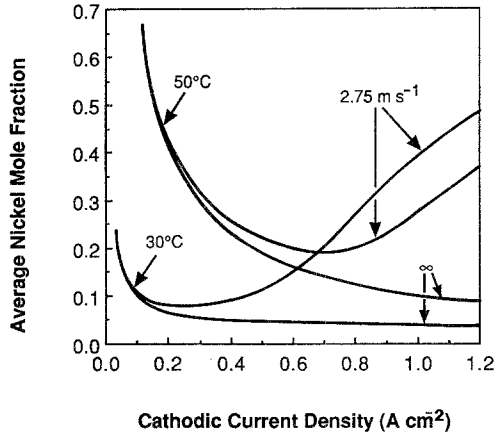

Fig. 4. Effect of the temperature and the average current density on the axially averaged nickel composition in the alloy for the modified Roehl bath. Results are shown for the secondary current distribution and for an electrolyte velocity of 2.75 m s^{-1}.

3.1.2. Effect of temperature. The effect of temperature and total current density on the alloy composition is seen in Fig. 4 for the modified Roehl bath. Results are shown for the secondary distribution case and for a characteristic velocity of 2.75 m s^{-1}. At current densities less than 0.3 A cm^{-2}, the effect of increasing the temperature at a given current is to increase the nickel content. In contrast, increasing the temperature in the tertiary range decreases the nickel content of the alloy.

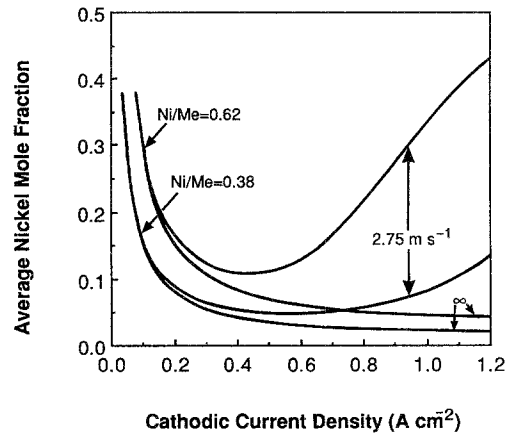

Fig. 5. Effect of the bath composition, at nickel-to-total metal ratios of 0.38 and 0.62, and the average current density on the axially averaged nickel composition in the alloy at 40° C. Results are shown for the secondary current distribution and for an electrolyte velocity of 2.75 m s^{-1}.

This is because the tertiary distribution composition is controlled primarily by the zinc mass transfer, which improves with increasing temperature. It should be noted that there is some uncertainty in the apparent activation energies used here, because they were estimated using a scheme that did not take into account the polarization data [6], as was later shown to be important [4].

3.1.3. Effect of bath composition. Figure 5 shows the effect of bath composition, total current density, and finite characteristic velocity on the average alloy composition. Results are plotted for the Roehl (Ni/Me = 0.38) and modified Roehl (Ni/Me = 0.62) baths. As expected the modified Roehl bath, with the higher nickel-to-total-metal ratio, consistently produces higher nickel composition in the deposit.

3.2. *Local nickel composition profiles*

Figure 6 shows the effects of characteristic velocity, temperature, bath composition, and total current density on the local composition profile of nickel along the electrode. The following conditions were used as the base case in each plot: average total current density, 0.8 A cm^{-2}; electrolyte velocity, 2.75 m s^{-1}; temperature, 40° C; and the modified Roehl bath (Ni/Me = 0.62). The transition to a uniform mass-transfer coefficient occurs from 10 to 30% of the way down the electrode, and the predicted composition of the alloy is a constant after this point. Therefore, only the profile from the first 30% of the cell is shown. Again, because the electrical resistance of the electrolyte dominates the mass-transfer and electrode-reaction resistance for all the conditions studied here, the calculated total current density distributions along the electrode are essentially uniform. On the other hand, partial current density distributions do vary in the axial direction as reflected in the non-uniform alloy composition predictions.

Each of the results show similar trends. As one proceeds along the length of the electrode, the zinc mass-transfer limitations become more severe and the nickel composition rises. The effect of each of the four

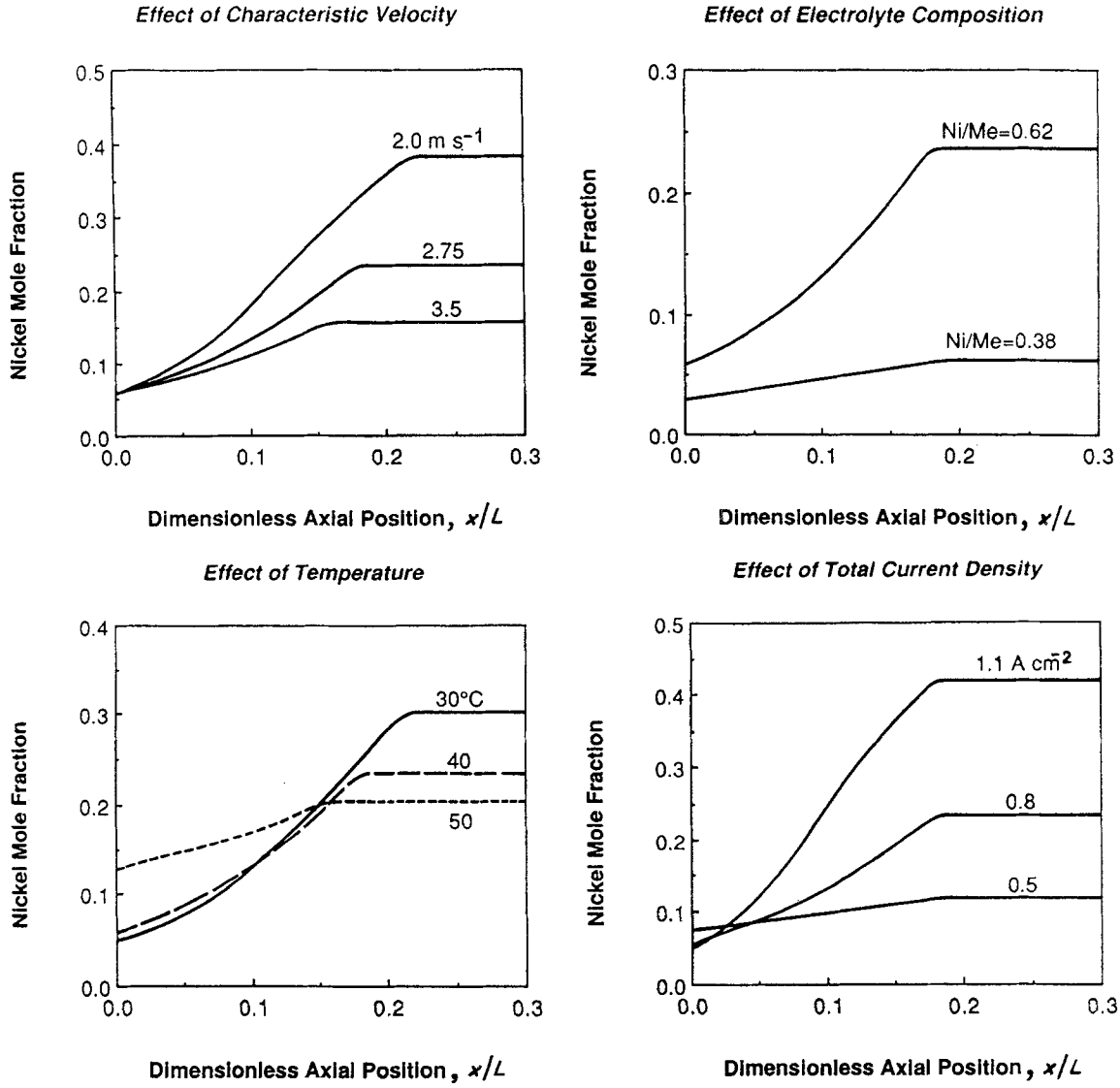

Fig. 6. Effect of characteristic velocity, temperature, bath composition, and total current density on the local nickel deposit composition profile in the parallel-plate cell. The base case, which is shown in each plot, is: modified Roehl bath, 40° C, characteristic velocity of 2.75 m s^{-1}, and average total current density of 0.8 A cm^{-2}.

variables on the overall nickel composition can be understood through their effects on the ratio of zinc partial current to the zinc limiting current. Increasing this ratio makes the zinc mass-transfer limitation more severe and results in a larger fraction of nickel in the alloy. Increasing the temperature, the zinc concentration, or the characteristic velocity and decreasing the current all lessen the severity of the zinc mass-transfer limitation and serve to decrease the total nickel composition in the deposit. These results agree well with those obtained experimentally by Tsuda *et al.* [16] for zinc–nickel deposition when the electrolyte was introduced into a parallel plate cell via a jet positioned at 45° relative to the cathode. An entrance region of approximately 10 times the equivalent diameter was observed as well as the trends shown in Fig. 6 for the effect of electrolyte velocity.

It is to be noted that in industrial cells in which the strip is moving, the effect of a non-uniform composition profile as shown above produces non-uniform alloy composition in the thickness direction of the deposit. This may be undesirable from the point of view of corrosion resistance, as the non-uniformities could lead to corrosion by galvanic action.

3.3. *Effect of varying the electrode gap*

In the gravity-flow cell, the gap between the anode and the cathode varies slightly from the top to the bottom of the cell. Because the interelectrode ohmic resistance dominates the other cell resistances, the local current density is highest where the gap is smallest and smallest where the gap is largest. This non-uniform current distribution is of little concern in electrogalvanizing, but it has the potential to result in non-uniform compositions in alloy plating. To investigate this, the effect of the non-uniform gap, S, was incorporated into the model. The current flux lines were considered to be perpendicular to the cathode, a valid approximation when the difference between the gaps at either end is small. The effect of the non-uniform gap on mass transfer was accounted for by using an axially varying value of d_e (twice the local gap) in the calculation of local boundary-layer thickness (Equation 15). The gap was taken to be 11 mm at the top of the cell and 9 mm at the bottom and to vary linearly in between.

On the down-pass in the gravity-flow cell, the strip enters the cell where the interelectrode gap is the widest and on the up-pass enters where the gap is the narrowest. Figure 7 shows the results for these two situations along with the parallel-plate case. The total current distribution predictions are shown in Fig. 7a, and they are seen to be essentially linear, varying to reflect the associated cell geometry.

The nickel composition profiles for these situations are shown in Fig. 7b. In the entrance region, the nickel composition is lower than the average because the zinc surface concentration has not been depleted to its downstream value. In the downsteam region, the nickel composition decreases with increasing local current density; increases in total current are carried primarily by the more kinetically facile zinc reaction.

4. Summary and conclusions

The results of this paper show that the uniformity of total current density in an industrial alloy-plating cell with a constant interelectrode gap does not necessarily imply uniformity of alloy composition along the electrode. Composition uniformity is achieved when the mass transfer is fast relative to the electrode kinetics so that the surface concentrations of the reacting species remain essentially at their bulk values. In such a case, the temperature and bath composition affect the average alloy composition through their influence on the electrode kinetics. However, under partial mass-transport control, because the mass-transfer efficiency is a function of position along the electrode, the resulting tertiary current distributions are non-uniform for the two metals. Consequently, the alloy composition becomes non-uniform, and the process variables affect the resulting alloy plate through their influence on the limiting mass-transfer rate.

For successful industrial zinc–nickel alloy plating, one desires high currents and uniform deposit compositions with 0.1 to 0.15 mole fraction nickel. The ideal nickel content versus current operating curve (like those given in Figs 3, 4, and 5) will have a flat region in the proper nickel composition region

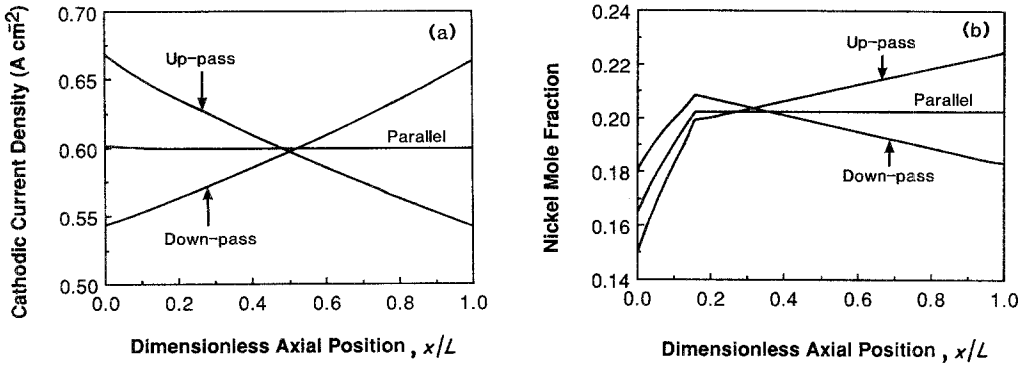

Fig. 7. Effect of varying the electrode gap and the cell entrance point on the current and alloy composition distribution along the electrode. The process variables are: minimum gap of 9 mm, maximum gap of 11 mm, modified Roehl bath, 50° C, inlet velocity of 2.75 m s^{-1}, and average total current density of 0.6 A cm^{-2}.

over all desired operating conditions. The results shown in Fig. 6, however, show that unless the concentrations of the zinc and nickel at the electrode surface are maintained close to their bulk values, the composition distribution within the cell will become non-uniform, resulting in composition non-uniformities through the thickness of the deposit even if the average composition is within specification. Increasing temperature, ion concentration, and characteristic velocity are expected to produce more uniform deposits.

It appears that the counter-flow design (Fig. 1a) is more favourable for alloy deposition than the gravity-flow cell. By injecting electrolyte counter to the strip direction on both the up-pass and the down-pass the mass-transfer rate can be increased, and both sides of the cell are expected to produce similar results. In the gravity-flow-cell, however, electrolyte flow is concurrent with the strip in one direction and countercurrent in the other. On the down-pass the velocity of the strip and the electrolyte are similar, and there is a risk based on the low characteristic velocity predictions of Fig. 4, that zinc will become severely mass-transfer-limited within the cell. In such a case, the alloy applied on the down-pass will be richer in nickel than that applied on the up-pass. The varying cell gap can also produce differences in composition on the up-pass and down-pass in some operating regions. However, when zinc is significantly mass-transfer-controlled, the effect of the varying gap on the mass transfer and the local current density tend to offset one another and lead to uniformity of alloy composition after the entrance length.

Because the geometry of the cells currently used for continuous strip plating is rather straightforward to analyse, the lack of useful kinetic data is the major obstacle to modelling alloy deposition processes. Once these parameters are determined, useful models of the cell behaviour are within reach. Kinetic parameters must be obtained for other systems of industrial interest, for example the zinc–nickel sulphate and zinc–iron systems, and work is needed to determine transport properties. The model introduced here provides a starting point from which further complexities of the situation can be investigated. For example, the hydrodynamics and mass transfer in an industrial cell are not well characterized. Specifically, the effects of electrolyte injection and gas evolution at both electrodes should be considered. Effective design, control, and optimization of continuous strip alloy plating processes will be achieved only when quantitative modelling such as that demonstrated here is combined with practical operating experience.

References

[1] J. W. Van Zee and E. J. Rudd, *J. Electrochem. Soc.* **135** (1988) 485C.
[2] E. J. Roehl, US Pat. 3,420,754 (1969).
[3] (a) T. Tsuda, K. Asano, M. Kimoto, A. Shibuya and S. Fujiwara, (b) W. A. Carter and R. L. Price, (c) H. N. Hahn, D. R. Vernon and K. Watanabe, (d) R. F. Higgs and W. R. Johnson, in *AESF Fourth Plating Symposium, May 5–7, 1987*, American Electroplaters and Surface Finishers Society, Orlando, Florida (1987).
[4] M. F. Mathias and T. W. Chapman, *J. Electrochem. Soc.* **137** (1990) 102.
[5] E. J. Roehl and R. H. Dillon, US Pat. 3,558,442 (1971).
[6] M. F. Mathias and T. W. Chapman, *J. Electrochem. Soc.* **134** (1987) 1408.
[7] S. A. Schukarev, L. S. Lilich and V. A. Latysheva, *Zh. Neorg. Khim.* **1** (1956) 225.
[8] 'Standard Potentials in Aqueous Solutions' (edited by A. J. Bard, R. Parsons and J. Jordan) Marcel Dekker, New York, Basel (1985) p. 787.
[9] D. J. Pickett and K. L. Ong, *Electrochim. Acta.* **19** (1974) 875.
[10] R. Higbie, *Trans. Am. Inst. Chem. Engr.* **31** (1935) 365.
[11] H. J. S. Sand, *Phil. Mag.* **1** (1901) 45.
[12] T. Tsuda, K. Asano and A. Shibuya, *Trans. Iron Steel Inst. Jpn* **26** (1986) 53.
[13] B. C. Sakiadis, *AIChE J.* **7** (1961) 26, 221.
[14] J. Newman, 'Electrochemical Systems', Prentice-Hall, Englewood Cliffs, NJ (1973) p. 230.
[15] 'Handbook of Mathematical Functions' (edited by M. Abramowitz and I. A. Stegun), Dover Publications, New York (1972) p. 920.
[16] T. Tsuda, A. Shibuya, M. Nishihara, F. Terasaki, K. Yamada, M. Katoh and K. Yanagi, presented at American Electroplaters Society SUR/FIN '84 Conference, New York (1984).